



Nanoimprinted perovskite metasurface for enhanced photoluminescence

HONGLEI WANG,¹ SHIH-CHIA LIU,² BALASUBRAMANIAM BALACHANDRAN,³ JIYOUNG MOON,¹ ROSS HAROLDSON,⁴ ZHITONG LI,¹ ARTUR ISHTEEV,⁵ QING GU,¹ WEIDONG ZHOU,² ANVAR ZAKHIDOV,^{4,5,6} AND WALTER HU^{1,7,*}

¹Department of Electrical and Computer Engineering, The University of Texas at Dallas, Richardson, TX 75080, USA

²Department of Electrical Engineering, The University of Texas at Arlington, Arlington, TX 76019, USA

³Department of Mechanical Engineering, The University of Texas at Dallas, Richardson, TX 75080, USA

⁴Department of Physics, The University of Texas at Dallas, Richardson, TX 75080, USA

⁵ITMO University, St. Petersburg, Moscow, Russia

⁶National University of Science and Technology, NUST "MISIS", Moscow, Russia

⁷ASIC and System State-key Lab, Microelectronics Department, Fudan University, Shanghai 200433, China

*walter.hu@utdallas.edu

Abstract: Recently, solution-processed hybrid halide perovskite has emerged as promising materials for advanced optoelectronic devices such as photovoltaics, photodetectors, light emitting diodes and lasers. In the mean time, all-dielectric metasurfaces with high-index materials have attracted attention due to their low-loss and high-efficient optical resonances. Because of its tunable by composition band gap in the visible frequencies, organolead halide perovskite could serve as a powerful platform for realizing high-index, low-loss metasurfaces. However, direct patterning of perovskite by lithography-based technique is not feasible due to material instability under moisture. Here we report novel organolead halide perovskite metasurfaces created by the cost-effective thermal nanoimprint technology. The nanoimprinted perovskite metasurface showed improved surface morphology and enhanced optical absorption properties. Significantly enhanced optical emission with an eight-fold enhancement in photoluminescence (PL) intensity was observed under room temperature. Temperature-dependent PL of perovskite nanograting metasurface was also investigated. Based on our results, we believe that thermal nanoimprint is a simple and cost-effective technique to fabricate perovskite-based metasurfaces, which could have broad impact on optoelectronic and photonic applications.

© 2017 Optical Society of America

OCIS codes: (220.4241) Nanostructure fabrication; (230.5298) Photonic crystals; (160.3918) Metamaterials; (350.2770) Gratings; (250.5230) Photoluminescence.

References and links

1. N. Yu and F. Capasso, "Flat optics with designer metasurfaces," *Nat. Mater.* **13**(2), 139–150 (2014).
2. A. Boltasseva and H. A. Atwater, "Materials science. Low-loss plasmonic metamaterials," *Science* **331**(6015), 290–291 (2011).
3. S. Jahani and Z. Jacob, "All-dielectric metamaterials," *Nat. Nanotechnol.* **11**(1), 23–36 (2016).
4. A. I. Kuznetsov, A. E. Miroshnichenko, M. L. Brongersma, Y. S. Kivshar, and B. Luk'yanchuk, "Optically resonant dielectric nanostructures," *Science* **354**(6314), aag2472 (2016).
5. Z.-J. Yang, R. Jiang, X. Zhuo, Y.-M. Xie, J. Wang, and H.-Q. Lin, "Dielectric nanoresonators for light manipulation," *Phys. Rep.* **701**, 1–50 (2017).
6. F. Aieta, M. A. Kats, P. Genevet, and F. Capasso, "Applied optics. Multiwavelength achromatic metasurfaces by dispersive phase compensation," *Science* **347**(6228), 1342–1345 (2015).
7. B. Shen, P. Wang, R. Polson, and R. Menon, "An integrated-nanophotonics polarization beamsplitter with $2.4 \times 2.4 \mu\text{m}^2$ footprint," *Nat. Photonics* **9**, 378–382 (2015).
8. I. Staude, V. V. Khadikov, N. T. Fofang, S. Liu, M. Decker, D. N. Neshev, T. S. Luk, I. Brener, and Y. S. Kivshar, "Shaping photoluminescence spectra with magnetoelectric resonances in all-dielectric nanoparticles," *ACS Photonics* **2**, 172–177 (2015).

9. A. Kojima, K. Teshima, Y. Shirai, and T. Miyasaka, "Organometal halide perovskites as visible-light sensitizers for photovoltaic cells," *J. Am. Chem. Soc.* **131**(17), 6050–6051 (2009).
10. K. A. Bush, A. F. Palmstrom, Z. J. Yu, M. Boccard, R. Cheacharoen, J. P. Mailoa, D. P. McMeekin, R. L. Z. Hoyer, C. D. Bailie, T. Leijtens, I. M. Peters, M. C. Minichetti, N. Rolston, R. Prasanna, S. Sofia, D. Harwood, W. Ma, F. Moghadam, H. J. Snaith, T. Buonassisi, Z. C. Holman, S. F. Bent, and M. D. McGehee, "23.6%-efficient monolithic perovskite/silicon tandem solar cells with improved stability," *Nat. Energy* **2**, 17009 (2017).
11. X. Hu, X. Zhang, L. Liang, J. Bao, S. Li, W. Yang, and Y. Xie, "High-performance flexible broadband photodetector based on organolead halide perovskite," *Adv. Funct. Mater.* **24**, 7373–7380 (2014).
12. L. Dou, Y. M. Yang, J. You, Z. Hong, W.-H. Chang, G. Li, and Y. Yang, "Solution-processed hybrid perovskite photodetectors with high detectivity," *Nat. Commun.* **5**, 5404 (2014).
13. H. Cho, S.-H. Jeong, M.-H. Park, Y.-H. Kim, C. Wolf, C.-L. Lee, J. H. Heo, A. Sadhanala, N. Myoung, S. Yoo, S. H. Im, R. H. Friend, and T.-W. Lee, "Overcoming the electroluminescence efficiency limitations of perovskite light-emitting diodes," *Science* **350**(6265), 1222–1225 (2015).
14. M. Yuan, L. N. Quan, R. Comin, G. Walters, R. Sabatini, O. Voznyy, S. Hoogland, Y. Zhao, E. M. Beauregard, P. Kanjanaboos, Z. Lu, D. H. Kim, and E. H. Sargent, "Perovskite energy funnels for efficient light-emitting diodes," *Nat. Nanotechnol.* **11**(10), 872–877 (2016).
15. G. Xing, N. Mathews, S. S. Lim, N. Yantara, X. Liu, D. Sabba, M. Grätzel, S. Mhaisalkar, and T. C. Sum, "Low-temperature solution-processed wavelength-tunable perovskites for lasing," *Nat. Mater.* **13**(5), 476–480 (2014).
16. H. Zhu, Y. Fu, F. Meng, X. Wu, Z. Gong, Q. Ding, M. V. Gustafsson, M. T. Trinh, S. Jin, and X. Y. Zhu, "Lead halide perovskite nanowire lasers with low lasing thresholds and high quality factors," *Nat. Mater.* **14**(6), 636–642 (2015).
17. M. A. Green, A. Ho-Baillie, and H. J. Snaith, "The emergence of perovskite solar cells," *Nat. Photonics* **8**, 506–514 (2014).
18. S. D. Stranks, G. E. Eperon, G. Grancini, C. Menelaou, M. J. P. Alcocer, T. Leijtens, L. M. Herz, A. Petrozza, and H. J. Snaith, "Electron-hole diffusion lengths exceeding 1 micrometer in an organometal trihalide perovskite absorber," *Science* **342**(6156), 341–344 (2013).
19. C. Wehrenfennig, G. E. Eperon, M. B. Johnston, H. J. Snaith, and L. M. Herz, "High charge carrier mobilities and lifetimes in organolead trihalide perovskites," *Adv. Mater.* **26**(10), 1584–1589 (2014).
20. N. J. Jeon, J. H. Noh, Y. C. Kim, W. S. Yang, S. Ryu, and S. I. Seok, "Solvent engineering for high-performance inorganic-organic hybrid perovskite solar cells," *Nat. Mater.* **13**(9), 897–903 (2014).
21. T. Leijtens, G. E. Eperon, N. K. Noel, S. N. Habisreutinger, A. Petrozza, and H. J. Snaith, "Stability of metal halide perovskite solar cells," *Adv. Energy Mater.* **5**, 1500963 (2015).
22. E. Horváth, M. Spina, Z. Szekrényes, K. Kamarás, R. Gaal, D. Gachet, and L. Forró, "Nanowires of methylammonium lead iodide ($\text{CH}_3\text{NH}_3\text{PbI}_3$) prepared by low temperature solution-mediated crystallization," *Nano Lett.* **14**(12), 6761–6766 (2014).
23. D. Zhang, Y. Yang, Y. Bekenstein, Y. Yu, N. A. Gibson, A. B. Wong, S. W. Eaton, N. Kornienko, Q. Kong, M. Lai, A. P. Alivisatos, S. R. Leone, and P. Yang, "Synthesis of composition tunable and highly luminescent cesium lead halide nanowires through anion-exchange reactions," *J. Am. Chem. Soc.* **138**(23), 7236–7239 (2016).
24. B. Gholipour, G. Adamo, D. Cortecchia, H. N. S. Krishnamoorthy, M. D. Birowosuto, N. I. Zheludev, and C. Soci, "Organometallic perovskite metasurfaces," *Adv. Mater.* **29**(9), 1604268 (2017).
25. Z. Y. Cheng, Z. Wang, R. B. Xing, Y. C. Han, and J. Lin, "Patterning and photoluminescent properties of perovskite-type organic/inorganic hybrid luminescent films by soft lithography," *Chem. Phys. Lett.* **376**, 481–486 (2003).
26. S. Chen, K. Roh, J. Lee, W. K. Chong, Y. Lu, N. Mathews, T. C. Sum, and A. Nurmikko, "A photonic crystal laser from solution based organo-lead iodide perovskite thin films," *ACS Nano* **10**(4), 3959–3967 (2016).
27. K. Meng, S. Gao, L. Wu, G. Wang, X. Liu, G. Chen, Z. Liu, and G. Chen, "Two-dimensional organic-inorganic hybrid perovskite photonic films," *Nano Lett.* **16**(7), 4166–4173 (2016).
28. H. Wang, R. Haroldson, B. Balachandran, A. Zakhidov, S. Sohal, J. Y. Chan, A. Zakhidov, and W. Hu, "Nanoimprinted perovskite nanograting photodetector with improved efficiency," *ACS Nano* **10**(12), 10921–10928 (2016).
29. S. V. Makarov, V. Milichko, E. V. Ushakova, M. Omelyanovich, A. Cerdan Pasaran, R. Haroldson, B. Balachandran, H. Wang, W. Hu, Y. S. Kivshar, and A. A. Zakhidov, "Multifold emission enhancement in nanoimprinted hybrid perovskite metasurfaces," *ACS Photonics* **4**, 728–735 (2017).
30. H. Yang, D. Zhao, S. Chuwongin, J.-H. Seo, W. Yang, Y. Shuai, J. Berggren, M. Hammar, Z. Ma, and W. Zhou, "Transfer-printed stacked nanomembrane lasers on silicon," *Nat. Photonics* **6**, 615–620 (2012).
31. D. Zhao, S. Liu, H. Yang, Z. Ma, C. Reuterskiöld-Hedlund, M. Hammar, and W. Zhou, "Printed large-area single-mode photonic crystal bandedge surface-emitting lasers on silicon," *Sci. Rep.* **6**, 18860 (2016).
32. A. Dualeh, N. Tétreault, T. Moehl, P. Gao, M. K. Nazeeruddin, and M. Grätzel, "Effect of annealing temperature on film morphology of organic-inorganic hybrid perovskite solid-state solar cells," *Adv. Funct. Mater.* **24**, 3250–3258 (2014).
33. J. Tauc, "Optical properties and electronic structure of amorphous Ge and Si," *Mater. Res. Bull.* **3**, 37–46 (1968).
34. A. E. Miroshnichenko, S. Flach, and Y. S. Kivshar, "Fano resonances in nanoscale structures," *Rev. Mod. Phys.* **82**, 2257–2298 (2010).

35. K. Wu, A. Bera, C. Ma, Y. Du, Y. Yang, L. Li, and T. Wu, "Temperature-dependent excitonic photoluminescence of hybrid organometal halide perovskite films," *Phys. Chem. Chem. Phys.* **16**(41), 22476–22481 (2014).
36. R. L. Milot, G. E. Eperon, H. J. Snaith, M. B. Johnston, and L. M. Herz, "Temperature-dependent charge-carrier dynamics in $\text{CH}_3\text{NH}_3\text{PbI}_3$ perovskite thin films," *Adv. Funct. Mater.* **25**, 6218–6227 (2015).

1. Introduction

Metasurfaces allow modulation of electromagnetic properties of natural materials to achieve special optical functionalities by sub-wavelength structure engineering [1]. Early realization of such artificial planar surfaces are based on noble plasmonic metals, which suffer from high energy dissipation due to ohmic losses, and, as a consequence, compromised device efficiency [2]. Recently, all-dielectric metasurfaces have attracted research interest due to use of various strong Mie-type resonances originated nanostructures as potentially low-loss platform [3–5]. A variety of functionalities such as optical wavefront molding [6], polarization beamsplitter [7], and enhanced photoluminescence [8] have been demonstrated on all-dielectric metasurfaces.

Recently, organolead halide-based perovskites have emerged as promising materials for optoelectronic applications such as photovoltaics [9, 10], photodetectors [11, 12], light emitting diodes [13, 14] and lasers [15, 16]. In particular, perovskite-based solar cells technology demonstrated remarkable advancement, with power conversion efficiency increased rapidly from 3.8% in 2009 [9] to 23.6% in early 2017 [10]. Such materials offer advantages of strong optical absorption [17], long carrier diffusion length [18], high carrier mobility [19], and broad wavelength tunability [15]. More importantly, perovskites are solution-processable which allows cost-effective fabrication [20]. Therefore, hybrid organo-halide perovskites could serve as powerful alternative materials for realizing high-index, low-loss all-dielectric metasurfaces. However, patterning nanostructures on perovskites is challenging as perovskites are incompatible with conventional lithography techniques ascribed to the material instability under moisture or solvents [21]. Therefore, currently reported perovskite nanostructures are usually created by chemical synthesis [22, 23], which lack dimension control and uniformity. Alternative patterning techniques have been utilized for hybrid perovskite such as focused ion beam [24] and soft lithography [25]. Perovskite photonic crystals were also reported based on template-assisted spin-coating process [26, 27]. Previously, we demonstrated successful thermal nanoimprinting of hybrid perovskite, which offers a cost-effective nanofabrication method for organo halide perovskite materials [28]. Nanoimprinted perovskites have demonstrated significantly improved efficiency for photodetectors [28] and sizable enhancement of photoluminescence *via* non-linear photoexcitation [29]. In this article, we investigate nanoimprinted perovskite with modeling based pre-designed nanograting metasurfaces both numerically and experimentally. We demonstrate strong modification of perovskite optical absorption and emission properties, which is useful for studying perovskite-based metadevices such as high-efficient light-emitting diodes and lasers.

2. Experiments

2.1 Nanoimprint mold patterning

The computer modeling based pre-designed silicon (Si) nanograting mold was fabricated by electron-beam lithography (EBL) with hydrogen silsesquioxane (HSQ) resist, followed by plasma etching for pattern transfer. A (100) lightly p-doped Si wafer was used and first ultrasonic cleaned with acetone and isopropanol (IPA). 30 nm thick HSQ (Dow Corning Co. XR1541 2%) film was spincoated on the Si substrates at 3000 r.p.m. for 60 s and baked at 90 °C for 5 mins. The EBL of HSQ gratings is done by a Raith 150-Two EBL tool at 30 KeV with a 30 μm aperture. 16 different patterns with a fixed periodicity of 350 nm in an area of 105 $\mu\text{m} \times 105 \mu\text{m}$ per pattern (300 periods) were formed. The nanograting width was varied

from ~80 nm to 130 nm. The HSQ patterns were developed in 20 wt % tetramethylammonium-hydroxide (TMAH) solution at 38 °C for 60s. Si substrate was etched to a depth of ~160 nm by inductively coupled plasma (ICP) with chlorine chemistry (Cl_2 50 sccm, DC power 50 W, ICP power 150 W, Plasma-Therm Versaline ICP system). Lastly, the remaining HSQ was removed by 20:1 buffered oxide etch (BOE) for 90s.

2.2 Perovskite thin film preparation

A modified solvent-engineering method reported by Jeon *et al.* [20] was used for methylammonium lead iodide (MAPbI_3) perovskite thin film deposition. This method utilizes a mixture of γ -butyrolactone (GBL) and $\text{N,N'$ -dimethylsulphoxide (DMSO) as perovskite solvents for spin-coating, followed by a toluene drip while spinning, which allows a formation of homogenous perovskite layer after thermal annealing. The MAPbI_3 perovskite solution was prepared by dissolving 1:1 molar ratio of PbI_2 and MAI in a 7:3 volume ratio of GBL: DMSO solvent mixture in a N_2 glovebox. The solution was heated at 60 °C for 24 hours, and the resulting MAPbI_3 concentration was 1.2 M. A glass substrate was used for the transmittance and reflectance measurements while Si substrate with 300 nm thermally grown oxide was used for PL measurements. The substrates were first ultrasonic cleaned with acetone and IPA and then treated by oxygen plasma. The MAPbI_3 precursor solution was then spincoated onto the substrates by a two-step process in a N_2 glovebox. 1000 r.p.m. and 5000 r.p.m. were used for the first and second spin-coating step respectively with each step lasting 22 s. During the second step, 350 mL of anhydrous toluene was added onto the film after 12 s. The film was then annealed on a hotplate at 100 °C for 10 mins to evaporate solvents, and a dense and uniform MAPbI_3 film was formed with a thickness of about 265 nm.

2.3 Nanoimprint process

In this study, both commercial Si nanograting mold (LightSmyth Technologies, SNS-C16.7-0808-350-D55-P) and the EBL fabricated pre-designed mold were used for nanoimprint lithography (NIL). The Si nanograting molds were first treated with an anti-adhesive monolayer 1H,1H,2H,2H-perfluorodecyltrichlorosilane (FDTS) in N-heptone solvent for 5 mins and then cleaned with acetone and IPA and blow dried with N_2 . The molds were then annealed at 100 °C for 20 mins. Perovskite metasurfaces were formed by thermal imprinting on the perovskite thin films, as illustrated in Fig. 1. The Si molds were brought into contact with the perovskite thin films on the SiO_2/Si substrates. The NIL was conducted using Obducat Nanoimprinter at 100 °C and 7 MPa for 20 mins. After imprint, the Si nanograting molds were carefully separated from perovskite samples via lift-off process. Perovskite nanograting metasurfaces were formed as the negative replications of the Si molds, as illustrated in Fig. 1(c).

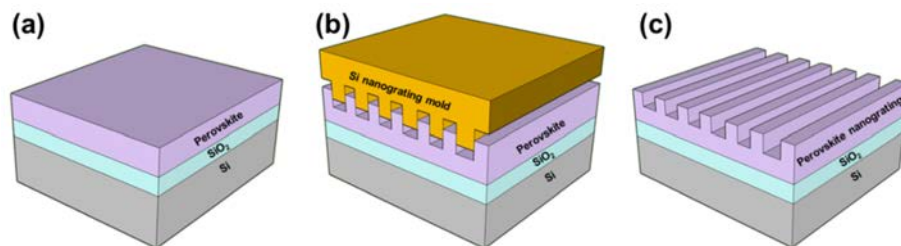


Fig. 1. Schematic nanoimprinting process flow to form perovskite nanograting metasurface: (a) spincoating perovskite thin films on the Si substrates with a thermal oxide layer, (b) thermal nanoimprint of perovskite with Si nanograting molds to form negative structure replications, and (c) after demolding, perovskite nanograting metasurfaces are formed.

2.4 Perovskite thin film and metasurface characterizations

The surface morphology, optical absorption, and emission of perovskite NIL metasurfaces were investigated in comparison with the reference thin films. A Zeiss Supra – 40 Scanning electron microscopy (SEM) system was used for surface morphology characterizations. A Perkin Elmer Lambda 900 spectrometer was used for the UV-Vis transmission and reflectance measurements, with perovskite thin film and NIL metasurface prepared on glass substrates. A micro-photoluminescence (μ PL) setup was employed for both low-temperature and room-temperature PL measurements [30, 31]. To evaluate the emission characteristics experimentally, the perovskite samples were first mounted on a temperature controlled stage inside a cryostat. The cryostat was connected with a vacuum pump and cool compressor to apply the designed operation temperature. A continuous wave (c.w.) green laser (532 nm) was used as the pump source incident from the surface normal direction via a long working distance objective lens ($\times 10$), and a spectrograph consisting of Horiba TRIAX320 monochromator and Electro-Optical Systems Inc. S-020-T1 silicon photodiode detector was used for spectral detection. The diameter of the excitation spot was around 110 μ m. The PL emitted light was then collected from the same objective lens separated with a cold mirror. The collected light was sent into the spectrograph.

3. Results and discussion

3.1 Nanoimprinted perovskite metasurface

As shown in Fig. 2(a), the perovskite thin film prepared by modified solvent engineering method demonstrated dense and uniform polycrystalline structures with grain size of a few hundred nanometers. The uniform perovskite nanograting structures after thermal NIL demonstrated high-fidelity replication of the Si nanograting mold [Fig. 2(b)]. The nanogratings have a patterned structure width of 270 nm and a periodicity of 600 nm. The results demonstrated that, although perovskites are crystalline solids without glass transition type behavior (unlike polymers), they could still be successfully patterned by thermal nanoimprint technology as they could be deformed and re-defined by mold hot embossing under sequential application of elevated pressure and temperature. In this study, a maximum pressure of up to 7 MPa was applied at a temperature of 100 °C which was reported to be optimal for perovskite annealing process [32]. Our results suggest that thermal NIL provides a simple and cost-effective method for nanofabrication of halide perovskite material metasurfaces.

The optical absorption properties of nanoimprinted perovskite were investigated by characterizing the transmittance [Fig. 2(c)] and reflectance [Fig. 2(d)] of perovskite films on glass substrates. The perovskite reference thin film has a thickness of 265 nm, and the imprinted metasurface has the grating period, width, depth, and residue thickness of 600 nm, 270 nm, 300 nm and 130 nm respectively. The NIL nanograting metasurface demonstrated significantly reduced transmittance over the entire spectrum and reduced reflectance for wavelength smaller than 930 nm. A transmission dip and reflection peak were observed on the nanograting metasurface at the wavelength around 1000 nm. The absorption of perovskite metasurface and reference thin film were calculated by $A = 1 - T - R$, where A is the absorption, T is the transmittance and R is the reflectance, assuming T and R equals the measured transmittance and reflectance values respectively. The resulting absorption spectra are presented in Fig. 2(e). The NIL metasurface demonstrated strong light trapping effect with significantly enhanced absorption for wavelength below 1050 nm. The absorption peak of the nanograting metasurface at the wavelength of 1015 nm is correlated with optical resonance due to metasurface structuring. The absorption value occasionally falls below zero for wavelength above 790 nm, which is caused by test error of transmittance and reflectance. The optical bandgap E_g of MAPbI₃ was determined by Tauc plot [33] - $(\alpha h\nu)^2$ versus $h\nu$ assuming direct allowed transition, where α is absorption coefficient and $h\nu$ is photon energy. As shown

in inset graph of Fig. 2(f), the linear extrapolation of perovskite thin film suggested a material bandgap of 1.58 eV (785 nm). The optical characterization results indicated the NIL metasurface modulates photonic band structure, density of states, as well as possibly improves inherent material properties (e.g. defect density). Such strong photon management effect could be utilized for photovoltaic as well as optoelectronic applications.

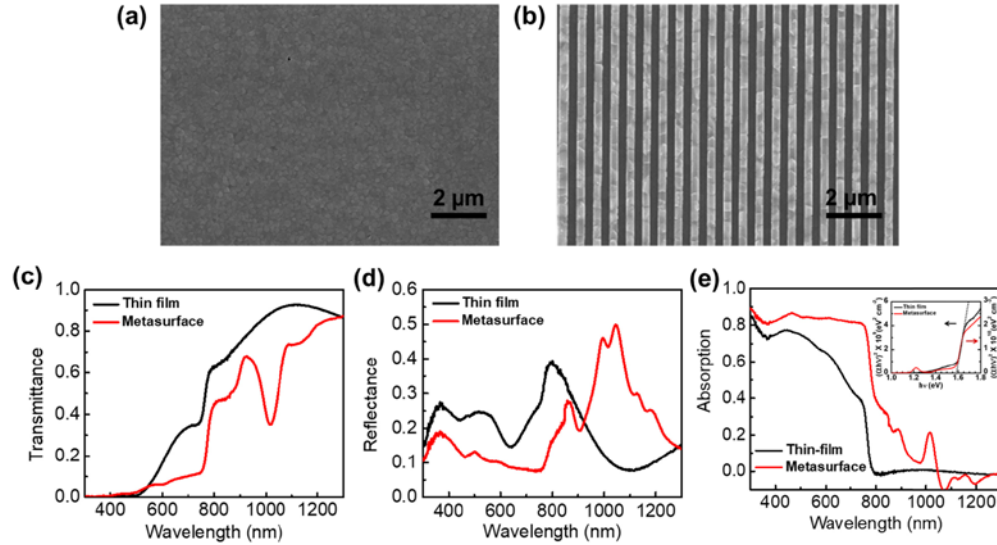


Fig. 2. Surface morphology and optical absorption properties of MAPbI₃ thin film and NIL metasurface. SEM images of surface morphology of (a) perovskite thin film prepared with modified solvent engineering method, and (b) NIL perovskite nanograting metasurface. (c) Transmittance, (d) reflectance and (e) calculated absorption spectra of perovskite reference thin film (thickness 265 nm), and NIL nanograting metasurface (period of 600 nm, structure width of 270 nm, and structure depth of 300 nm with 130 nm residue thickness). The inset of (e) is plot of $(\alpha h\nu)^2$ versus $h\nu$ for direct transitions in MAPbI₃ thin film and metasurface, where α is absorption coefficient and $h\nu$ is photon energy. The perovskite optical bandgap E_g is obtained by extrapolation to $(\alpha h\nu)^2 = 0$.

3.2 Numerical simulation of perovskite metasurface

Enhanced emission is expected by perovskite metasurface geometry optimization for optical cavity resonance. Numerical simulation of perovskite nanograting metasurface was conducted using the finite-difference time-domain (FDTD) method. Figure 3(a) illustrates the cross-section view of metasurface structure consisting of Si substrate, silicon oxide layer, and perovskite nanograting layer. An optimal cavity geometry was found by simulation as shown in Fig. 3(a), i.e. grating period of 350 nm, trench width of 105 nm, trench depth of 160 nm, and residue thickness of 160 nm, on 300 nm thick oxide layer. Figure 3(b) illustrates the calculated optical transmission spectrum of the structure depicted in Fig. 3(a), where several dips are observed in the wavelength range between 700 nm to 840 nm. The blue-solid lines represent the transverse electric (TE, s) and red-dashed lines the transverse magnetic (TM, p) polarizations. Two sharp dips around 710 nm (A_p , TM polarization) and 790 nm (B_s , TE polarization) indicated the existence of high-quality (Q) cavity modes. The Q factors are obtained by Fano fitting [34] the guided resonances in transmission spectra. The cavity Q factors of A_p and B_s modes were calculated to be 3.9×10^3 and 5.2×10^3 , respectively. Note that infinite grating length with only radiation loss was considered. Figure 3(c) shows simulated electrical field distribution distribution along the z-axis direction for highest- Q factor mode B_s under oblique incidence of 0.5° . The field maximums were observed in perovskite close to the trench bottom corner.

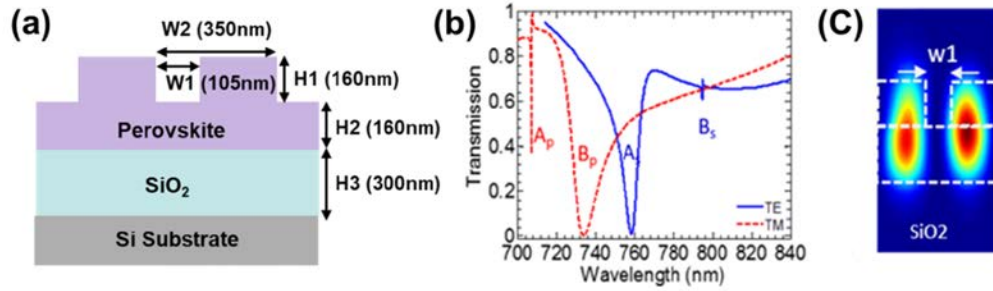


Fig. 3. Schematic and numerical simulations of MAPbI₃ nanograting metasurface. (a) Schematic structure cross-section with an optimal geometry. The corresponding simulated results of (b) optical transmission spectrum and (c) electrical field distribution for the highest- Q mode B_s.

3.3 Photoluminescence enhancement

To achieve the best enhanced emission from perovskite metasurface, we fabricated custom Si nanograting molds and made the NIL metasurface structures according to the simulated optimal geometry as shown in Fig. 3(a). Perovskite nanogratings of 300 periods over a patterned area of $105\ \mu\text{m} \times 105\ \mu\text{m}$ were fabricated. A variety of patterns formed with a fixed periodicity of 350 nm, but varied grating width between ~ 80 to 130 nm. The surface morphology of a typical NIL MAPbI₃ metasurface is illustrated in Fig. 4(a), with the corresponding mold pattern shown in the inset image. The mold pattern was negatively replicated on the perovskite films, with the 105 nm wide-grating structure of the Si mold transferred to the trench of perovskite.

The optical emission properties of the perovskite reference thin films and NIL nanograting metasurfaces were characterized. The room-temperature PL results are presented in Fig. 4(b). The perovskite reference thin film shows a PL peak wavelength at 763 nm with a full width at half maximum (FWHM) of 44 nm. The PL peak shows a positive deviation of 50 meV from Tauc plot assuming direct bandgap, which likely results from UV-Vis or PL measurement error or MAPbI₃ unusual band structures or charge carrier dynamics where controversies existed. Significant improved PL properties were observed with perovskite imprinted nanograting metasurface. The metasurface with a periodicity of 350 nm and trench width of 105 nm demonstrated a 6-fold improvement of PL intensity and a 2-fold reduction of FWHM, while a higher performance with an 8-fold enhancement of PL intensity was correlated with a periodicity of 350 nm and a larger trench width of 125 nm. The result slightly deviated from our numerical simulation possibly due to non-uniformity, defects, or dimensional variation in the imprinted samples. Two narrow amplified spontaneous emission (ASE) peaks at wavelengths around 780 nm and 810 nm were identified in the PL spectrum, which were corresponded to the cavity mode A_s (TE, 760 nm) and B_s (TE, 790 nm) in Fig. 3(b) respectively. The red shift of PL peaks compared to the simulation was ascribed to the possible difference of material refractive index (a constant refractive index of 2.5 was used in simulation) and structural dimensions (uniform distributions of grating width and straight grating sidewall were assumed in simulation). Despite of its lower Q factor compared to B_s mode, A_s mode contributed to stronger ASE due to higher material gain at 780 nm. Small blue shifts of ASE peaks were observed by increasing trench width from 105 nm to 125 nm. Besides the optical cavity resonance, NIL metasurface shows improved photon absorption [Fig. 2(c)-2(e)], increased local density of states [29] and improved carrier lifetime [28], which could also contribute to the PL enhancement. Further emission improvement is expected by optimizing the geometry design to tune the highest- Q factor mode into the center of material gain spectrum, and optimizing fabrication process to acquire better control on structure size (e.g. imprint depth) and surface morphology (e.g. sidewall roughness).

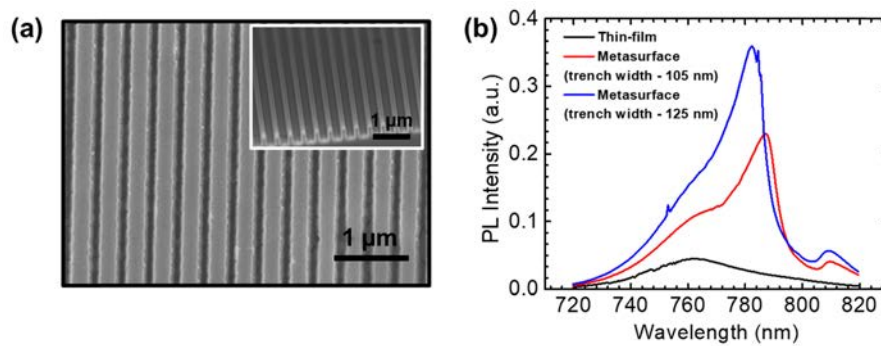


Fig. 4. Surface morphology and optical emission properties of MAPbI_3 thin film and NIL nanograting metasurface. (a) SEM of perovskite nanograting metasurface fabricated according to numerical simulation results – periodicity of 350 nm, trench width and depth of 105 nm and 100 nm respectively, with a residue thickness of 200 nm, inset shows the corresponding Si nanograting mold. (b) Steady-state PL spectra of perovskite thin film (thickness 265 nm) and NIL nanograting metasurface with a trench width of 105 nm (red) and 125 nm (blue), a periodicity of 350 nm and a depth around 100 nm with a residue thickness of 200 nm, pumped with a laser power of 0.3 mW at room temperature.

The temperature-dependent PL spectra of perovskite reference thin film [Fig. 5(a)] and NIL nanograting metasurface [Fig. 5(b)] were further characterized. As illustrated in Fig. 5(a), as the temperature decreases, the PL intensity increased along with reduced linewidth, accommodated by red shift of emission peak. These behaviors were also demonstrated in the plot of PL intensity *versus* temperature [Fig. 5(c)] and PL peak wavelength *versus* temperature [Fig. 5(d)], in which over 22-fold intensity improvement and a peak shift from 763 nm to 785 nm were correlated with the temperature decreasing from 300 K to 100 K. The red shift, while unconventional in semiconductor materials, has been reported on hybrid perovskite materials [35, 36]. The bandgap energy of perovskite has positive relationship with temperature within same crystallographic phase, which is ascribed to the interplay between electron-phonon renormalization and thermal expansion [35]. An additional PL peak at wavelength around 740 nm emerged at a temperature of 100 K, which resulted from the structural phase change of MAPbI_3 from tetragonal to orthorhombic that contributed to a significant blue shift in PL spectra. The dual PL peaks indicated the coexistence of crystallographic phases at 100 K for perovskite prepared by the modified solvent engineering method. The results generally agree well with other solution-processed perovskite thin films measured under low-temperature [35, 36]. The imprinted nanograting metasurface demonstrated some temperature-dependent behaviors similar to reference thin film such as increased intensity with reduced linewidth by decreasing temperature, as well as the emergence of phase-transition-related PL peak at 740 nm under a temperature of 100 K [Fig. 5(b)]. A ~6-fold PL intensity enhancement as temperature decreasing from 300 K to 100 K was revealed for nanograting metasurface in Fig. 5(c). Gradual red shift of PL peak from 780 nm to 786 nm was observed for temperature decreasing from 300 K to 150 K, while a significant blue shift to 768 nm occurred under a temperature of 100 K [Fig. 5(d)]. This blue shift should be attributed to arose of strong cavity resonance corresponding to the TM mode B_p . As temperature decreases, the gain spectrum blue shifts while the ASE peaks corresponding to mode A_s and B_s red shifts. Therefore, the B_p mode (768 nm) acquired higher material gain than A_s mode (792 nm) at 100 K, contributing to the sharp ASE peak [Fig. 5(b)]. Figure 5(e) illustrated the power-dependent PL spectrum of imprinted metasurface at 100 K, in which spectrum narrowing at B_p mode was observed with FWHM reduced from 32 nm to 12 nm as power increases from 0.01 mW to 0.2 mW. The PL intensity enhancement of metasurface compared to thin film was suppressed under low temperature. This is because although material gain increases as temperature decrease, the blue shift of the gain spectrum

in combination with the red shift of the mode wavelength results in a net reduction in optical gain for the A_s mode. Meanwhile, the PL peak at 100 K was correlated with B_p mode with lower Q -factor. Further improvement is expected by geometry optimization for emission wavelength tuning of high- Q factor modes.

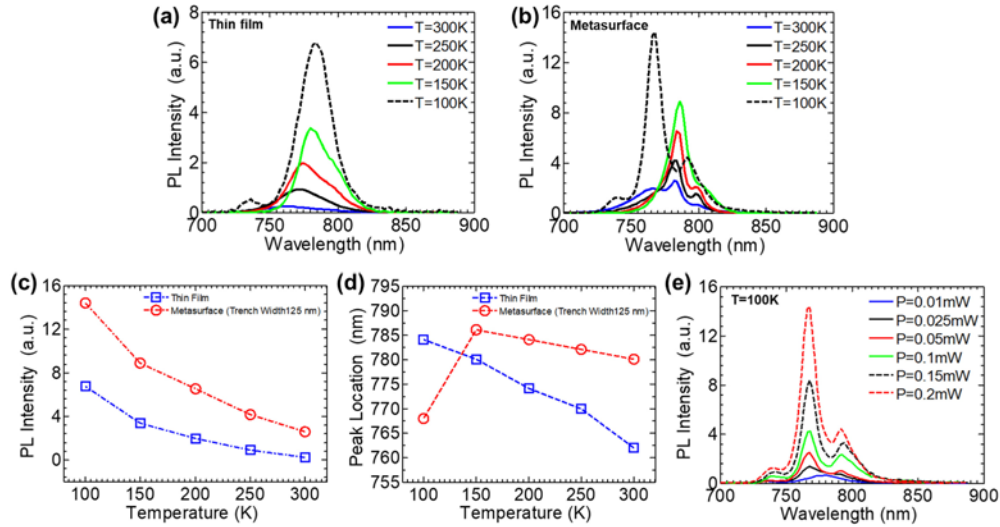


Fig. 5. Temperature-dependent PL characteristics of MAPbI_3 reference thin film and NIL nanograting metasurface with a trench width of 125 nm. PL spectra of (a) thin film and (b) NIL nanograting metasurface with a temperature ranging from 300 K to 100 K, pumped with a power of 0.2 mW. Plots of (c) PL intensity versus temperature and (d) PL peak wavelength versus temperature for both reference thin film and NIL nanograting metasurface. (e) Power-dependent PL spectra of NIL nanograting metasurface at a temperature of 100 K.

4. Summary and conclusions

In summary, hybrid organohalide perovskite metasurfaces have been formed by thermal nanoimprint. The NIL perovskite metasurfaces revealed excellent morphology with high-fidelity replication of the Si nanograting mold. The halide perovskite nanograting metasurfaces demonstrated significantly enhanced morphology with higher crystallinity and larger grain sizes and optical absorption properties compared with the reference thin film surfaces. Numerical calculation indicated emission improvement is feasible *via* metasurface geometry optimization for better dielectric resonances. The optimized metasurface with smaller periodicity of 350 nm as compared to earlier studied 600 nm was constructed by nanoimprinting using a newly designed Si nanograting mold, which is house fabricated by e-beam lithography and plasma etching. Amplified spontaneous emission has been observed with an 8-fold enhancement of PL intensity. Such enhancement is due to photonic crystal cavity resonance by the proper metasurface design as well as improved photon absorption and longer carrier lifetime due to nanoimprinting. Temperature-dependent PL measurements of NIL perovskite metasurface demonstrated similar spectral evolution as the perovskite thin films – a general red shift accommodated by increased PL intensity and reduced linewidth by decreasing temperature, with additional PL peak indicating coexistence of crystallographic phases at a low temperature of ~ 100 K. A blue shift of PL peak was observed on NIL nanograting metasurface at 100 K, ascribing to the emergence of strong ASE relating to a new cavity mode with higher material gain. Further metasurface emission enhancement is expected by improving metasurface design, mold fabrication and nanoimprinting process. We believe that thermal NIL is a simple and cost-effective method for patterning large-scale, low-loss and high-index organo-halide perovskite metasurfaces, which is useful for perovskite

optoelectronic and photonic metadevices such as high-efficient LEDs, photodetectors, photovoltaics cells and lasers.

Funding

National Science Foundation (NSF) (CBET-1606141, ECCS-0955027); Welch Foundation (AT-1617); Chinese National Science Foundation (CNSF) (61628402); Ministry of Education and Science of the Russian Federation in the framework of Megagrant (14. Y26.31.0010) for optical measurements and *via* Increased Competitiveness Program of NUST (K2-2015-014) for sample preparation.